# CO$_2$ methanation over Ni-promoted mesostructured silica nanoparticles: Influence of Ni loading and water vapor on activity and response surface methodology studies

M.A.A. Aziz [a], A.A. Jalil [a,b], S. Triwahyono [c,*], M.W.A. Saad [b]

[a] Institute of Hydrogen Economy, Universiti Teknologi Malaysia, 81310 UTM Johor Bahru, Johor, Malaysia
[b] Department of Chemical Engineering, Faculty of Chemical Engineering, Universiti Teknologi Malaysia, 81310 UTM Johor Bahru, Johor, Malaysia
[c] Department of Chemistry, Faculty of Science, Universiti Teknologi Malaysia, 81310 UTM Johor Bahru, Johor, Malaysia

HIGHLIGHTS

- CO$_2$ methanation is dependence to the Ni loading (1–10 wt.%) on MSN.
- The order of reaction activity was 10Ni/MSN $\approx$ 5Ni/MSN > 3Ni/MSN > 1Ni/MSN.
- 0.5 vol% water vapor in the feed gave a negative effect on the CO$_2$ methanation.
- Water vapor suppressed carbonyl species on the surface of Ni/MSN.
- 85% conversion of CO$_2$ was achieved over 5Ni/MSN under the optimum condition by RSM.

GRAPHICAL ABSTRACT
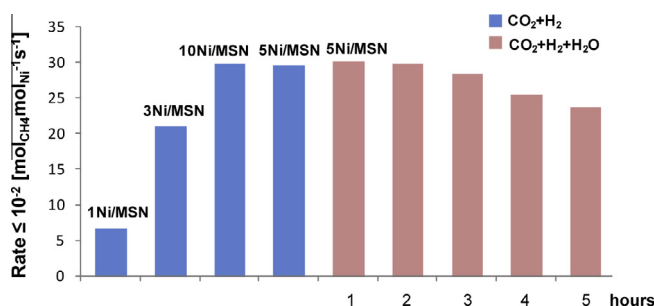
ABSTRACT

The effects of Ni loading and water vapor on the properties of Ni/mesoporous silica nanoparticles (MSN) and CO$_2$ methanation were studied. X-ray diffraction, N$_2$ adsorption–desorption, and pyrrole-adsorbed infrared (IR) spectroscopy results indicated that the increasing Ni loading (1–10 wt.%) decreased the crystallinity, surface area, and basic sites of the catalysts. The activity of CO$_2$ methanation followed the order of 10Ni/MSN $\approx$ 5Ni/MSN > 3Ni/MSN > 1Ni/MSN. These results showed that the balance between Ni and the basic-site concentration is vital for the high activity of CO$_2$ methanation. All Ni/MSN catalysts exhibited a high stability at 623 K for more than 100 h. The presence of water vapor in the feed stream induced a negative effect on the activity of CO$_2$ methanation. The water vapor decreased the carbonyl species concentration on the surface of Ni/MSN, as evidenced by CO + H$_2$O-adsorbed IR spectroscopy. The response surface methodology experiments were designed with face-centered central composite design (FCCCD) by applying 2$^4$ factorial points, 8 axial points, and 2 replicates, with one response variable (CO$_2$ conversion). The Pareto chart indicated that the reaction temperature had the largest effect for all responses. The optimum CO$_2$ conversion was predicted from the response surface analysis as 85% at an operating treatment time of 6 h, reaction temperature of 614 K, gas hourly space velocity (GHSV) of 69105 mL g$_{cat}^{-1}$ h$^{-1}$, and H$_2$/CO$_2$ ratio of 3.68.

© 2014 Elsevier B.V. All rights reserved.

* Corresponding author. Tel.: +60 7 5536076; fax: +60 7 5536080.
  E-mail address: sugeng@utm.my (S. Triwahyono).

## 1. Introduction

The conversion of $CO_2$ to methane transforms a molecule (hydrogen) that is difficult to store and transport into a molecule (methane) that is relatively easy to store and can be transported millions of miles in existing natural-gas pipelines. As most hydrogen today is produced from fossil hydrocarbons, its conversion to methane is not a sensible idea unless an inexpensive and renewable source of hydrogen is found (e.g. biomass or water). The hydrogenation of $CO_2$ or methanation is scientifically interesting as it might teach us about activating $CO_2$, which is a topic of great current interest [1–9]. This reaction is also called the Sabatier reaction as follow:

$$CO_2(g) + 4H_2(g) \rightarrow CH_4(g) + 2H_2O(g) \quad \Delta G^o_{298\ K} = -27\ kcal\ mol^{-1}$$
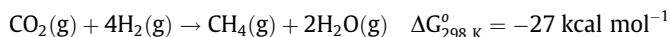
The catalysts employed are concentrated on Ni-based catalysts. Ni-based catalysts are more promising in industrial applications, owing to their much lower cost. However, Ni-based catalysts are not selective and are subject to coking [10], which lowers the efficiency of methanation. Catalytic selectivity and stability of Ni catalysts are affected by many factors such as nickel loading, promoters, supports, catalyst preparation procedure, and experimental conditions. In this study, we focus on the effects of nickel loading on the catalytic behaviors of Ni catalysts, because the nickel loading significantly affects the dispersion of nickel species on supports. The nickel loading on the support affected both the interaction of nickel with the support and the nickel dispersion on the support (Ni particle sizes), which further affected the catalytic behaviors during methanation. In general, the metal species tend to be highly dispersed across the carrier at low metal loadings, whereas the metal particles tend to aggregate at high metal loadings, forming large particles. Understanding this relationship can help researchers to understand dispersion–activity relationships and prepare active, selective, and stable Ni catalysts. Mesostructured silica nanoparticles (MSN) represent a potential support, which has a high surface area and contains acidic/basic features [5,11–13]. These properties can enhance the adsorption of $CO_2$ onto the support surface. Hence, MSN are selected as support materials in this study.

Recently, we proposed nickel/MSN-based catalysts, which demonstrate high activity and selectivity for $CO_2$ methanation [5]. This present paper focuses on the effects of Ni loading and water vapor on the performance of Ni/MSN catalysts in $CO_2$ methanation. Furthermore, the optimum conditions for $CO_2$ methanation over Ni/MSN were identified by response surface methodology (RSM). Catalytic properties and characterization data are discussed using X-ray diffraction (XRD), $N_2$ adsorption–desorption, and pyrrole-adsorbed Fourier-transform infrared (FTIR) spectroscopy techniques.

## 2. Experimental

### 2.1. Catalyst preparation

MSN was prepared by sol–gel method according to the report by Karim et al. [14]. The surfactant cetyltrimethylammonium bromide (CTAB; Merck), ethylene glycol (EG; Merck) and $NH_4OH$ solution (QRec) were dissolved in water with the following molar composition of $CTAB:EG:NH_4OH:H_2O = 0.0032:0.2:0.2:0.1$. After vigorous stirring for about 30 min at 353 K, 1.2 mmol of tetraethyl orthosilicate (Merck) and 1 mmol of 3-aminopropyl triethoxysilane (Merck) were added to the clear mixture to give a white suspension solution. This solution was then stirred for another 2 h, and the samples were collected by centrifugation at 20,000 rpm.

The synthesized MSN were dried at 333 K and calcined at 823 K for 3 h in air to remove the surfactant.

Supported Ni catalysts were prepared by impregnation of MSN powder with an aqueous solution of Ni salt precursor, $Ni(NO_3)_2$ (Merck, 99%). The resulting slurry was heated slowly at 353 K under continuous stirring and maintained at that temperature until nearly all the water being evaporated. The solid residue was dried in an oven at 383 K overnight before calcination at 823 K for 3 h in air. The metal loading of the catalysts thus prepared was 1, 3, 5 and 10 wt.%.

### 2.2. Characterization

The crystalline structure of the catalyst was determined with X-ray diffraction (XRD) recorded on a powder diffractometer (Bruker Advance D8, 40 kV, 40 mA) using a Cu Kα radiation source in the range of $2\theta = 1.5–90°$. The primary crystallite size of NiO ($D_{NiO}$) was calculated by means of the Scherrer equation [15]:

$$D_{NiO} = \frac{0.9\lambda}{B\cos\theta} \tag{1}$$

where $\lambda$ is the X-ray wavelength corresponding to Cu-Kα radiation (0.15406 nm), $B$ is the broadening (in radians) of the nickel (2 0 0) reflection and $\theta$ is the angle of diffraction corresponding to peak broadening. The BET analysis of the catalyst was determined by $N_2$ adsorption–desorption isotherms using a Quantachrome Autosorb-1 instrument. The catalyst was outgassed at 573 K for 3 h before being subjected to $N_2$ adsorption. Pore size distributions and pore volumes were determined from the sorption isotherms using a non localized density functional theory (NLDFT) method. In the FTIR measurements, pyrrole has been used as a probe molecule for the characterization of basic sites. The measurements were performed on an Agilent Cary 640 FTIR spectrometer equipped with a high-temperature stainless steel cell with $CaF_2$ windows. Prior to the measurements, 30 mg of sample in the form of a self-supported wafer was reduced in $H_2$ stream (100 ml/min) at 773 K for 4 h and cooling to 303 K under He atmosphere. For pyrrole adsorption, the reduced catalyst was exposed to 2 Torr of pyrrole at 303 K for 30 min, followed by outgassing at 423 K for 30 min. All spectra of pyrrole adsorption were recorded at room temperature with a spectral resolution of 5 $cm^{-1}$ with five scans.

### 2.3. Catalytic activity measurements

$CO_2$ methanation was conducted in a fixed-bed quartz reactor with an interior diameter of 8 mm at atmospheric pressure at temperature range of 373–723 K. The thermocouple was directly inserted into the catalyst bed to measure the actual pretreatment and reaction temperatures. The catalyst was sieved and selected in the 20–40 μm fraction. Initially, 200 mg of catalyst were treated in an oxygen stream ($F_{Oxygen} = 100$ ml/min) for 1 h followed by a hydrogen stream ($F_{Hydrogen} = 100$ ml/min) for 4 h at 773 K and cooled down to the desired reaction temperature in a hydrogen stream. After the temperature became stable, a mixture of $H_2$ and $CO_2$ was fed into the reactor at a specific gas hourly space velocity (GHSV) and $H_2/CO_2$ mass ratio. All gases were controlled with calibrated mass flow controllers (SEC-400 MK2, Stec Ltd., Japan). The activity was monitored with decreasing temperature and back to verify stable catalyst conditions during these measurements. The composition of the outlet gases was analyzed with an on-line 6090 N Agilent gas chromatograph equipped with a GS-Carbon PLOT column and a TCD detector. The lines from the outlet of the reactor to the GC were heated at 383 K to avoid condensation of the products. The moisture trap was installed at the outlet gas line of the reactor to prevent moisture from entering the GC. The influence of water vapor on $CO_2$ methanation was carried

out by injecting a specific amount of water into a steel capillary. This capillary was heated by a resistance wire and water was subjected to evaporation. The water vapor and the gases $H_2$ and $CO_2$ were premixed. The composition of water vapor in the stream was 0.5 vol% and the reaction was performed at 673 K. For the research surface methodology (RSM) analysis, catalytic reactions were performed with different reaction variables based on the face-centred central composite design (FCCCD) method. To determine the activity and selectivity, the products were collected after 1 h of steady-state operation at each temperature. The conversion of carbon dioxide, selectivity of products and rate of methane formation were calculated by the following equations:

$$X_{CO_2}(\%) = \frac{F_{CO_2,in} - F_{CO_2,out}}{F_{CO_2,in}} \times 100\% \qquad (2)$$

$$S_x(\%) = \frac{F_{x,out}}{F_{CO_2,in} - F_{CO_2,out}} \times 100\% \qquad (3)$$

$$rate\ (s^{-1}) = \frac{F_{x,out}}{mole\ of\ Ni_{Total}} \qquad (4)$$

where $X_{CO_2}$ is the conversion of carbon dioxide (%), $S_x$ is the selectivity of $x$ product (%) in which $x$ is a $CH_4$ or CO, $F$ is a molar flow rate of $CO_2$ or product in mole per second.

## 2.4. Experimental design and optimization

In this study, statistical analysis of $CO_2$ methanation was performed using Statsoft Statistica 8.0 software. The FCCCD was used to study the interaction of process variables and to predict the optimum process condition for $CO_2$ methanation by applying RSM. Independent variables considered important were gas hourly space velocity ($X_1$), treatment time ($X_2$), reaction temperature ($X_3$) and hydrogen to carbon dioxide ratio, $H_2/CO_2$ ($X_4$). Treatment time is referred to the time used during the treatment process under hydrogen stream prior to the reaction. The range and coded level of the $CO_2$ methanation process variables studied are listed in Table S1 (supplementary data). The independent variables were coded to the $(-1, 1)$ interval where the low and high levels were coded as $-1$ and $+1$, respectively. According to FCCCD, the total number of experiments conducted is 26 with 24 factorial points, 8 axial points and 2 replicates at the center points. The $CO_2$ conversion ($Y$) was taken as the response of the design experiment. The experimental design and corresponding results of three responses are listed in Table S2 (supplementary data). The full quadratic models for $CO_2$ conversion is given as the following equation:

$$\begin{aligned} Y_i = {} & \beta_o + \beta_1 X_1 + \beta_2 X_2 + \beta_3 X_3 + \beta_4 X_4 + \beta_{12} X_1 X_2 + \beta_{13} X_1 X_3 \\ & + \beta_{14} X_1 X_4 + \beta_{23} X_2 X_3 + \beta_{24} X_2 X_4 + \beta_{34} X_3 X_4 + \beta_{11} X_1^2 \\ & + \beta_{22} X_2^2 + \beta_{33} X_3^3 + \beta_{44} X_4^4 \end{aligned} \qquad (5)$$

where $Y_i$ is the predicted response $i$ whilst $X_1$, $X_2$, $X_3$ and $X_4$ are the coded form of independent variables. The term $\beta_o$ is the offset term; $\beta_1$, $\beta_2$, $\beta_3$ and $\beta_4$ are the linear terms; $\beta_{11}$, $\beta_{22}$, $\beta_{33}$ and $\beta_{44}$ are the quadratic terms; and $\beta_{12}$, $\beta_{13}$, $\beta_{14}$, $\beta_{23}$, $\beta_{24}$, $\beta_{34}$ are the interaction terms.

The equation model was tested with the analysis of variance (ANOVA) with 5% level of significant. The ANOVA was used to checking the significance of the second-order models and it is determined by $F$-value. Generally, the calculated $F$-value should be greater than tabulated $F$-value to reject the null hypothesis, where all the regression coefficients are zero. The calculated $F$-value is defined as the following equation:

$$F_{value} = \frac{MS_{SSR}}{MS_{SSE}} \qquad (6)$$

where $MS_{SSR}$ and $MS_{SSE}$ are mean of square regression and mean of square residual, respectively. The $MS_{SSR}$ and $MS_{SSE}$ were obtained by dividing sum of squares (SSR) and sum of residual (SSE) over degree of freedom (DF), respectively. Meanwhile, tabulated $F$-value was obtained from $F$ distribution based on DF for regression and residual, respectively at a specific level of significance, $\alpha$-value [16].

## 3. Results and discussion

### 3.1. Characterization of catalysts

Fig. 1A shows the small-angle XRD patterns of MSN and Ni-based MSN catalysts. The patterns exhibit three peaks, indexed as (1 0 0), (1 1 0), and (2 0 0) which are reflections of typical two-dimensional, hexagonally ordered mesostructures (*p6mm*), demonstrating the high quality of the mesopore packing. The ordered MSN support structure was disturbed markedly by the introduction of Ni. No shift in the peaks was observed, but the intensities decreased with increasing Ni loading in the order MSN > 1Ni/MSN > 3Ni/MSN > 5Ni/MSN > 10Ni/MSN, indicating structural degradation of MSN. The presence of Ni crystallites on the catalysts were characterized using wide-angle XRD (30°–90°), as shown in Fig. 1B, in which the diffraction peaks at 37.3°, 43.2°, 62.9°, 75.3°, and 79.4° can be attributed to face-centered cubic crystalline NiO. The peaks were more intense with increasing Ni loading from 1 to 10 wt.%, corresponding to a more crystalline phase of NiO on the MSN support.

The porosity of the catalysts was measured by the $N_2$ physisorption method. It is well understood that the location of the inflection point is related to a pore in the mesoscale and that the sharpness of these curves reveals the uniformity of the mesopore size distribution [17]. Fig. 2A and B show the adsorption–desorption isotherms and pore size distribution, respectively, for all catalysts. All isotherm curves, except 10Ni/MSN, exhibited two capillary condensation steps. The first step, in a relative pressure range of $P/P_o = 0.3$–0.4, was attributed to the nitrogen condensation that took place in the internal mesopores. There was no hysteresis loop in this capillary condensation. The second step, above $P/P_o = 0.95$ in the adsorption branch, was due to the presence of interparticle voids. A small hysteresis loop at this relative pressure was ascribed to the condensation of nitrogen within the interstitial voids or to the interparticle textural porosity created by MSN particles, which indirectly reflects the size of particles, that is, a higher partial pressure was associated with a smaller particle size. However, upon increasing the Ni loading from 1 to 10 wt.%, both capillary condensation steps were decreased simultaneously. For 10Ni/MSN, the first step almost disappeared, whereas the second step decreased by almost 40%. The increasing of Ni loading on MSN also affected
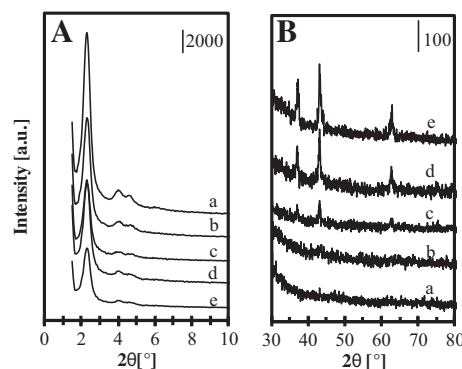


**Fig. 1.** Low-angle (A) and wide-angle (B) XRD patterns of (a) MSN, (b) 1Ni/MSN, (c) 3Ni/MSN, (d) 5Ni/MSN and (e) 10Ni/MSN.
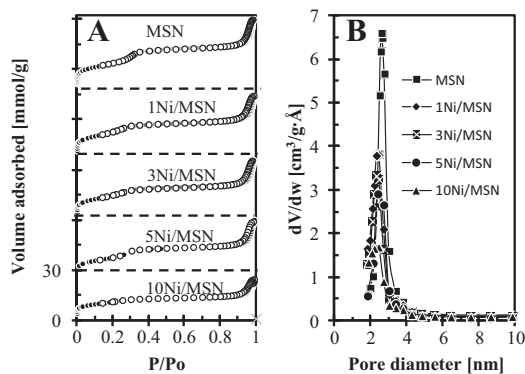
**Fig. 2.** (A) $N_2$ adsorption–desorption isotherm and (B) pore size distribution of all catalysts.

the pore distribution of the catalysts (Fig. 2B), in which the highest distributions of pore diameters were observed at about 2.8 nm. The introduction of 1 wt.% Ni on MSN decreased the cumulative pore distribution by 40%, whereas a 70% reduction was observed on 10Ni/MSN. Textural parameters of MSN and Ni/MSN catalysts are summarized in Table 1. For bare MSN, the BET surface area was 1051 $m^2 \, g^{-1}$. However, the introduction of Ni from 1 to 10 wt.% decreased the surface area from 926 to 662 $m^2 \, g^{-1}$, respectively, indicating that the pores of the MSN support are filled by dispersing nickel oxides [18]. Although the results of the total pore volume measurements showed inconsistency upon Ni loading, the average pore diameter increased as the Ni loading increased from 1 to 10 wt.%. Such great differences between nickel-containing and non-nickel samples can be explained by the isomorphous substitution of nickel atoms into the silica frameworks. This leads to a significant contraction of the walls and, consequently, expansion of the pores [19].

Reduced MSN and Ni/MSN catalysts possessed an intense band at 3740 $cm^{-1}$ with a shoulder at 3710 $cm^{-1}$ and a broad halo centered around 3650 $cm^{-1}$ (Fig. 3A). The bands at 3740 and 3710 $cm^{-1}$ are unambiguously assigned to terminal (isolated) and internal silanol groups, respectively. The broad absorbance is indicative of the presence of H-bonded hydroxyl groups. From these results, as the Ni loading increased from 1 to 10 wt.%, the concentration of silanol reduced simultaneously, suggesting a perturbation of the silica framework upon interaction with NiO. Fig. 3 also reported FTIR pyrrole adsorption with two spectral regions: 3800–3000 $cm^{-1}$ (Fig. 3B) and 2200–1300 $cm^{-1}$ (Fig. 3C). The background spectrum of the original, activated at 773 K, is subtracted. In the first region, the main broad band, situated at about 3475–3200 $cm^{-1}$, can be assigned to the N–H stretching vibrations of chemisorbed pyrrole ($C_4H_4NH$) interacting with the basic sites of framework oxygen atoms. The H-donor pyrrole properties allowed the formation of $C_4H_4NH$–O bridges with basic oxygen. In these cases, the band at 3530 $cm^{-1}$ indicates the position of a pyrrole N–H band in the gas phase [20] and the band at 3410 $cm^{-1}$ indicates physisorbed pyrrole in a liquid-like state [21], where the N–H group interacts with the π-system of another pyrrole molecule. The band at 3467 $cm^{-1}$ is attributed to the perturbed N–H stretch of pyrrole molecules interacting with the surface of basic sites. In the region of 2200–1300 $cm^{-1}$, the ring-stretching vibrations of adsorbed pyrrole show the complexity of the recorded IR spectra, which show a series of bands at 1851, 1685, 1581, 1535, 1469, 1423, and 1388 $cm^{-1}$. Nevertheless, among these bands, two intense bands at 1535 and 1423 $cm^{-1}$ are observed, which are attributed to the formation of non-dissociated pyrrole hydrogen bound to basic $O^{2-}$ [22]. Upon increasing the Ni loading from 1 to 10 wt.%, all bands decreased, particularly the band at 3467 $cm^{-1}$, indicating that the introduction of Ni reduced the basic sites of the catalyst. MSN and 10Ni/MSN catalysts showed the highest and lowest basic site concentration, respectively. Differences in the relative intensity of the IR bands for pyrrole

**Table 1**
Physical properties of fresh and spent catalysts.

| Catalyst | BET surface area ($m^2 \, g^{-1}$) | | Total pore volume ($cm^3 \, g^{-1}$) | | Average pore diameter (nm) | | Ni particle size (nm)[a] |
|---|---|---|---|---|---|---|---|
| | Fresh | Spent | Fresh | Spent | Fresh | Spent | |
| MSN | 1051 | – | 0.758 | – | 2.8 | – | – |
| 1Ni/MSN | 926 | 139 | 0.602 | 0.443 | 2.8 | 12.7 | 2.1 |
| 3Ni/MSN | 850 | 324 | 0.711 | 0.606 | 2.9 | 7.5 | 5.3 |
| 5Ni/MSN | 879 | 124 | 0.798 | 0.339 | 3.4 | 10.9 | 9.9 |
| 10Ni/MSN | 662 | 372 | 0.643 | 0.493 | 3.5 | 5.3 | 12.4 |

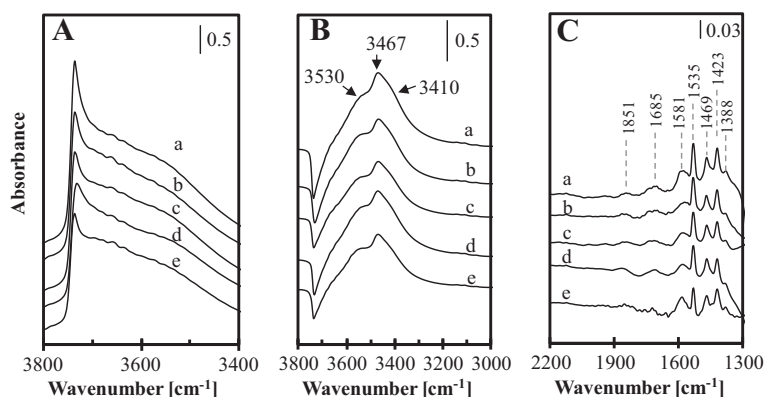[a] Determined by XRD (Debye-Sherrer method).



**Fig. 3.** (A) IR spectra after activated at 773 K and normalized IR spectra of pyrrole adsorbed on reduced catalysts after outgassing at 423 K in the range of (B) 3800–3000 $cm^{-1}$ and (C) 2200–1300 $cm^{-1}$ for the catalysts (a) MSN, (b) 1Ni/MSN, (c) 3Ni/MSN, (d) 5Ni/MSN and (e) 10Ni/MSN.
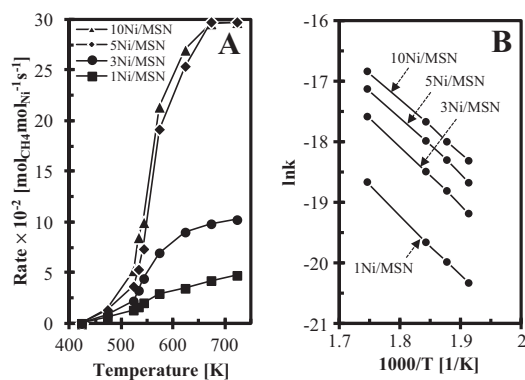
**Fig. 4.** (A) Effect of Ni loading on MSN for $CO_2$ methanation at steady state condition as a function of reaction temperature at GHSV = 50,000 mL $g_{cat}^{-1}$ $h^{-1}$ and $H_2/CO_2$ = 4/1. (B) Arrhenius plot for $CO_2$ methanation over Ni/MSN in the temperature range 523–573 K.

adsorption may be attributed to the different morphology of the nickel particles [23]. Therefore, it could be suggested that the decrease in intensity of the IR bands after increasing the Ni loading from 1 to 10 wt.% was caused by the presence of a bulk Ni phase. This is evidenced by the XRD patterns, which show the presence of NiO bulk, which increased from 2.1 to 12.4 nm for 1Ni/MSN to 10Ni/MSN.

### 3.2. Catalytic performance

The effect of Ni loading on $CO_2$ methanation over Ni/MSN was investigated and the results are summarized in Fig. 4 and Table 2, where the rate of methane formation ($mol_{CH_4}$ $mol_{Ni}^{-1}$ $s^{-1}$) is plotted as a function of reaction temperature in the range of 373–723 K. S-curve results were observed for all catalysts, indicating that the production rate for methane was not influenced by intraparticle diffusion of the catalysts under the reaction conditions. Furthermore, it was observed that the order of activity for $CO_2$ methanation at 673 K was 10Ni/MSN ≈ 5Ni/MSN > 3Ni/MSN > 1Ni/MSN. However, 10Ni/MSN exhibited a better result at low temperature (<623 K) compared to 5Ni/MSN. For 5Ni/MSN and 10Ni/MSN, the reaction began at 473 K and the conversion reached 100% at 673 and 723 K, respectively. $CO_2$ methanation increased rapidly at 523 K over both of these catalysts. Indeed, 3Ni/MSN, 5Ni/MSN, and 10Ni/MSN could catalyze $CO_2$ methanation at and below 473 K, whereas 1Ni/MSN started to be active at 523 K and reached 13.6% conversion at 673 K. Regarding the product selectivity, the major products were always methane; no $C_2$ or heavier hydrocarbons were observed in this experiment. At a similar conversion level ($X_{CO_2}$ = 20%), >99% of methane and a trace amount CO byproduct were observed over 5Ni/MSN. However, 100% selectivity to methane was observed for 1Ni/MSN, 3Ni/MSN, and 10Ni/MSN. In contrast, Kwak et al. reported a different trend, in which metal loadings exceeding 5 wt.% promoted 100% selectivity to methane



**Fig. 5.** Stability test of all catalysts. Reaction temperature = 623 K, $H_2/CO_2$ = 4/1, GHSV = 50,000 mL $g_{cat}^{-1}$ $h^{-1}$.

over the Rh/$Al_2O_3$ system [4]. The discrepancy in the results may be attributed to the metal phase on the support. For the Ni/MSN system, the Ni phase was observed in the bulk and/or sintered phase, and this could promote highly selective methane production in the reaction. In contrast, in the Ru/$Al_2O_3$ system reported by Kwak et al., low selectivity to methane was observed when the Ru metal was in an atomically pure phase on the support. The selectivity to methane achieved 100% when the Ru loading was increased to 10 wt.%, which was attributed to the sintered phase of Ru on the $Al_2O_3$ support [4]. The activation energy ($E_a$) (Fig. 4B) of the catalysts depends, to a large extent, on the amount of Ni loading on the MSN, and $E_a$ values of 74–83 kJ $mol^{-1}$ were calculated in a low temperature range for all Ni-based catalysts, which followed the order 1Ni/MSN > 3Ni/MSN > 5Ni/MSN > 10Ni/MSN.

The stability tests of all catalysts are shown in Fig. 5, where the conversion of $CO_2$ is plotted as a function of the time-on-stream. In order to keep $CO_2$ conversion lower than 100%, the reaction was carried out at 623 K. The activities were maintained for more than 100 h. After stability testing, all spent catalysts were subjected to $N_2$ adsorption–desorption in order to study their properties. The spent catalysts of Ni/MSN showed a decrease in surface area, total pore volume, and average pore diameter. The decrease may be due to the undesirable carbon deposition on the pores of catalyst during the methanation which originated not only from CO disproportionation, but also from $CH_4$ decomposition [24]. However, the decrease of those properties gave a little effect on the activity of the catalysts. This may be due to the large amount of active surface area which were still remained although the surface area was decreased after 100 h of reaction. As the activity of 5Ni/MSN was among the highest toward $CO_2$ methanation at 623 K, this catalyst was used in subsequent studies to understand the effect of water vapor on the reaction and RSM.

### 3.3. Effect of water vapor on the methanation reaction

In the methanation of $CO_2$, a considerable amount of water is formed. It has been found that the use of two reactors connected

**Table 2**
$CO_2$ methanation over Ni/MSN at GHSV = 50,000 mL $g_{cat}^{-1}$ $h^{-1}$ and $H_2/CO_2$ = 4/1.

| Catalyst | Rate[a] $\times 10^{-2}$ ($mol_{CH_4}$ $mol_{Ni}^{-1}$ $s^{-1}$) | | Conversion (%)[a] | Selectivity (%)[b] | | $E_a$ (kJ $mol^{-1}$)[c] |
|---|---|---|---|---|---|---|
| | $T$ = 473 K | $T$ = 623 K | | $CH_4$ | CO | |
| 1Ni/MSN | 0.26 | 3.45 | 11 | 100 | 0 | 83 |
| 3Ni/MSN | 0.79 | 9.00 | 29 | 100 | 0 | 79 |
| 5Ni/MSN | 1.33 | 25.38 | 82 | 99.9 | 0.1 | 76 |
| 10Ni/MSN | 1.38 | 27.02 | 85 | 100 | 0 | 74 |

[a] Reaction condition: $T$ = 623 K, $H_2/CO_2$ = 4/1, GHSV = 50,000 mL $g_{cat}^{-1}$ $h^{-1}$.
[b] Selectivity at similar conversion level, $X_{CO_2}$ = 20%.
[c] $E_a$ values were determined in the range of 523–573 K.

in series, in which water formed in the first reactor, which was removed before passing into the second reactor, is effective in increasing the conversion of $CO_2$ into methane. In addition, in the fuel processors, the reformate gases in the stream contain considerable amounts of steam, which may affect $CO_x$ methanation characteristics. In order to investigate the water tolerance of the catalyst, water vapor was added to the feed and the results that were obtained over 5Ni/MSN are summarized in Fig. 6A. From these results, the activity was shown to be reduced by 30% after 5 h exposure to water vapor. Batista et al. [2] also reported the same trend on $CO_2$ methanation over the Co/γ-$Al_2O_3$ system, in which the reaction did not occur appreciably in the presence of water. Therefore, it is suggested that the presence of water in the feed stream has a negative effect on $CO_2$ methanation over the Ni/MSN system. The negative effect was possibly due to the formation of $CO_2$ through the water gas shift (WGS) reaction between intermediate CO and the excess of water. Moreover, water vapor significantly accelerates the rate of sintering of Ni and enhances the collapse of the support, as reported by Bartholomew et al. [1]. The structure collapse of MSN may be occurs mechanochemically through the hydrolysis of Si—O—Si bond in the presence of adsorbed water due to its hydrophilicity [25]. Konaya et al. had reported the effect of water vapor on Si-MCM-48 system and found that the collapse of the structure was accompanied by a remarkable increase in the Q3 and Q2 silicate peaks as evidenced by $^{29}$Si MAS NMR spectra. The molar ratios of Q2/Q3/Q4 was 7.6/46/46 after the 10-day moisture treatment. Thus presumably Si—O—Si bonds were hydrolyzed, resulting in the decrease in the regularity [26].

The effect of water vapor on the intermediate CO was explained based on the results of FTIR for CO and $H_2O$ adsorption, as presented in Fig. 6B. Three bands were observed at 2040, 1913, and 1627 $cm^{-1}$. The first two bands were attributed to the carbonyl species, whereas the third was attributed to adsorbed water. A slight decrease in the band intensities at 2040 and 1913 $cm^{-1}$ indicates the decreasing amount of carbonyl species on the surface of the catalyst. This is attributed to the presence of water vapor, which interacts with some of the carbonyl species through the WGS reaction. On the other hand, the band of water at 1627 $cm^{-1}$ increased, owing to the introduction of water vapor into the system. Although the present reactor conditions were in a single reactor, the result shows the importance of two series reactors, which is economical and can be applied at the industrial level.

### 3.4. RSM analysis

RSM is a method used to determine the optimum conditions of a process, and it allows users to gather large amounts of informa-
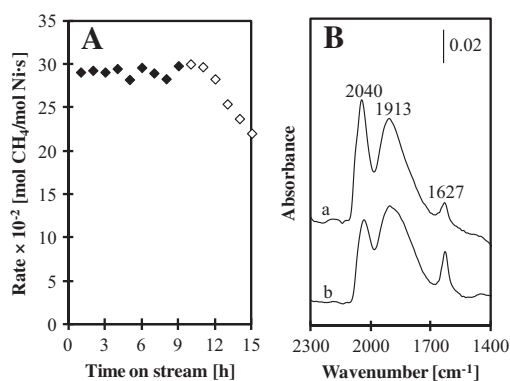


**Fig. 6.** (A) Activity of $CO_2$ methanation over 5Ni/MSN at 673 K in the absence (◆) and in the presence (◇) of water vapor in the feed. (B) FTIR adsorption of CO on 5Ni/MSN at 303 K (a) followed by the adsorption of water vapor at 303 K (b).

tion from a small number of experiments. It is also possible to observe the relationships between variables and responses, and has been successfully applied to a wide range of chemical reactions involving more than one response [27]. Based on RSM analysis, the quadratic model for $CO_2$ conversion is presented in Eq. (7):

$$Y = 71.379 - 1.948X_1 + 0.5476X_1^2 + 3X_2 - 1.6171X_2^2$$
$$+ 33.7987X_3 - 20.9524X_3^2 - 1.0531X_4 - 8.4524X_4^2$$
$$- 0.1604X_1X_2 - 0.125X_1X_3 - 0.5X_1X_4 + 0.9403X_2X_3$$
$$+ 0.1106X_2X_4 - X_3X_4 \qquad (7)$$

Fig. S1 (supplementary data) compares the observed value of $CO_2$ conversion with the predicted value obtained from Eq. (7). The coefficient of determination ($R^2$) for $CO_2$ conversion is 0.9919, indicating 99.19% of the variability in the data is accounted for by the model. According to Haaland [28], the empirical model is adequate to explain most of the variability in the essay reading, which should be at least 0.75 or greater. Table S3 (supplementary data) shows the analysis of variance (ANOVA) of the regression parameters for the predicted response surface quadratic model. As the model value ($F = 97.115$) exceeds the table value ($F_{(14,11,0.05)} = 2.7186$) and has a low probability value ($P > F < 0$), the Fisher $F$-test demonstrated that the experimental results fitted well, indicating that the model was significant. In addition, values of $P > F < 0.05$ indicate that the model terms are significant, whereas values greater than 0.10 indicate that the model terms are not significant. Fig. S2 (supplementary data) shows the $t$-distribution values in a Pareto chart and the corresponding $p$-values of the variables in Eq. (7). The $p$-values serve as a tool to check the significance of each coefficient. The corresponding coefficient with a smaller $p$-value or a $t$-value with a greater magnitude donates more significance into the model. The largest effect on $CO_2$ conversion is the linear term of reaction temperature ($X_3$), which has the smallest $p$-value (0.000000) and the largest $t$-value (33.4390) at the 95% significance level. In addition, the quadratic term for reaction temperature ($X_3^2$), the quadratic term of the $H_2/CO_2$ ratio ($X_4^2$), and the linear term for the treatment time ($X_2$) could be regarded as significant factors in affecting the $CO_2$ conversion, owing to the large $t$-values of −7.8212, −3.1551, and 2.9689, respectively. The rest of the factors could be considered less significant in affecting the $CO_2$ conversion, as their $p$-values were higher than 0.05.

Response surfaces and contour plots are generally used to evaluate relationships between parameters and to predict results under given conditions. However, it is complicated to analyze the interaction between parameters in this study, owing to the presence of many interaction terms. Instead, the response surfaces and contour plots were used to optimize the conditions of the $CO_2$ methanation over 5Ni/MSN. Six 3D RSM plots between four parameters were constructed for the $CO_2$ conversion model (Fig. 7), and they were plotted as a function of two of the factors while the others were maintained constant at their mean levels. The interaction between the corresponding variables was negligible when the contour of the response surface was circular. On the contrary, interactions between the relevant variables were significant when the contour of the response surfaces was elliptical. Notably, only the contour plots in Fig. 7A–C were elliptical, indicating significant interaction effects between the parameters studied.

Fig. 7A shows the response surface plot, demonstrating the effects of the reaction temperature and treatment time on $CO_2$ conversion. From the analysis of the response surface plot, the reaction temperature exhibited a more significant influence on the response surface in comparison to treatment time, which can also be explained by the Pareto chart (Fig. S2), showing a larger $t$-value for the reaction temperature (33.4390) compared to the treatment time (2.9689). $CO_2$ conversion significantly increases with
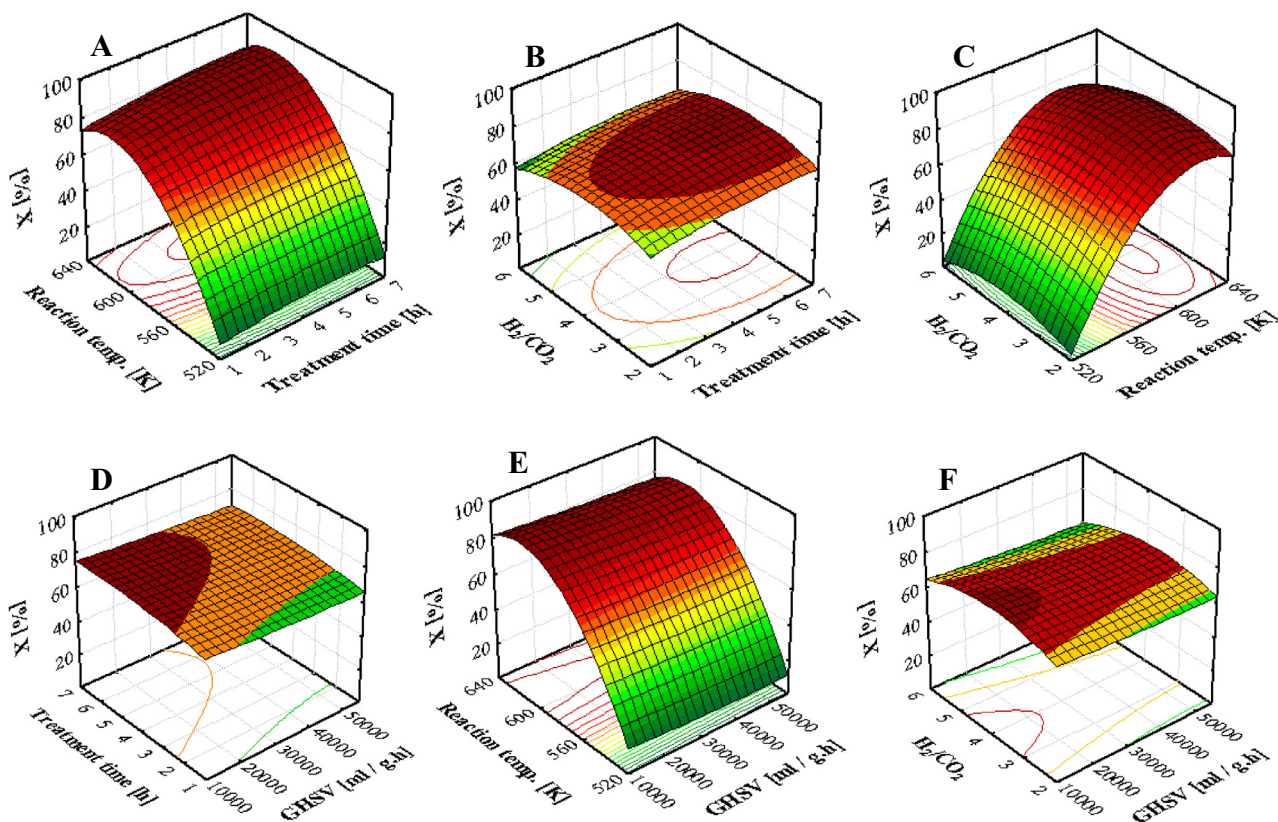
**Fig. 7.** Response surface plot of the combined (A) reaction temperature and treatment time, (B) $H_2/CO_2$ ratio and treatment time, (C) $H_2/CO_2$ ratio and reaction temperature. (D) Treatment time and GHSV, (E) reaction temperature and GHSV and (F) GHSV and $H_2/CO_2$ ratio on $CO_2$ conversion.

increasing reaction temperature and slightly decreases after the maximum at 614 K is reached, owing to the thermodynamic barrier that is reached. In addition, the slight decrease in $CO_2$ conversion with increasing temperature can be associated with the effect of site blockage by the formation of larger amounts of inactive surface carbon at higher temperatures [29]. The reverse water gas shift (RWGS) reaction may also be a factor in decreasing the $CO_2$ conversion when the temperature is increased to more than 614 K [3]. Therefore, it is important to develop selective $CO_2$ methanation catalysts characterized by high activity at sufficiently low temperatures, which are able to retard both RWGS reactions. At constant reaction temperature, the $CO_2$ conversion increases as the treatment time is increased to 6 h. This behavior may be related to changes in the number of surface Ni metal atoms, owing to an increase in the treatment time. According to the mechanism of $CO_2$ methanation [5], the metallic Ni sites are responsible for dissociating hydrogen to form atomic hydrogen. The atomic hydrogen then interacted with the carbon species to form methane. Thus, an increase in metal sites (i.e.: Ni sites) will result in an increase in the $CO_2$ conversion to methane process.

The effects of the $H_2/CO_2$ ratio and treatment time on $CO_2$ conversion are shown in Fig. 7B. The $CO_2$ conversion over the catalyst showed a volcano-shaped trend with respect to the $H_2/CO_2$ ratio. Increasing the $H_2/CO_2$ ratio produced a positive effect on the activity up to $H_2/CO_2$ ratio of 3.68:1 and then slightly decreased up to a $H_2/CO_2$ ratio of 7:1. The effect can be explained by the larger t-value of the $H_2/CO_2$ ratio (−3.1551) compared to the treatment time (2.9689) (Fig. S2). The increase and decrease in $CO_2$ conversion as a function of $H_2/CO_2$ ratio at constant treatment time may be due to the change in the amount of molecular hydrogen in the reaction stream. The optimum ratio of $H_2/CO_2 = 3.68:1$ contains a suitable amount of molecular hydrogen, in which the adsorbed hydrogen on the catalyst simultaneously

hydrogenates the carbon species on the surface of the catalyst to form methane.

Fig. 7C represents the effects of the $H_2/CO_2$ ratio at constant reaction temperature on $CO_2$ conversion. From the analysis of the response surface plot, the reaction temperature exhibited a significant influence on the response surface in comparison to the $H_2/CO_2$ ratio, which can also be clarified by the larger t-value of the reaction temperature (33.4390) compared to the $H_2/CO_2$ ratio (−3.1551) (Fig. S2). All of the parameters studied were found to affect $CO_2$ conversion. However, from the analysis, it appears that the reaction temperature is the dominant factor in $CO_2$ conversion, possibly owing to its strong relationship with the formation of methane. Additionally, it can be explained by the largest t-value of reaction temperature (33.4390) (Fig. S2), indicating the most significant effect on $CO_2$ conversion. Therefore, optimum $CO_2$ conversion predicted from the response surface analysis is 85% at an operating treatment time of 6 h, reaction temperature of 614 K, GHSV of 69,105 mL $g_{cat}^{-1}$ $h^{-1}$, and $H_2/CO_2$ ratio of 3.68. An additional experiment was carried out to validate the optimization results obtained by response surface analysis. The experiment and predicted $CO_2$ conversion at optimum conditions is shown in Table S4 (supplementary data). The differences between the predicted and observed values are 3.5%, which is considered small, as the observed values are within the 5% level of significance.

## 4. Conclusion

The study of the Ni loading on the properties of Ni/MSN catalysts and $CO_2$ methanation showed that increasing the Ni loading (1–10 wt.%) decreased the crystallinity, surface area, and number of basic sites in the catalysts, as evidenced by XRD, $N_2$ adsorption–desorption, and pyrrole-adsorbed IR spectroscopy results,

respectively. The activity of $CO_2$ methanation followed the order $10Ni/MSN \approx 5Ni/MSN > 3Ni/MSN > 1Ni/MSN$. The data showed that a balance between the Ni and basic site concentrations is vital for high $CO_2$ methanation activity. All Ni/MSN catalysts gave a good stability at 623 K for more than 100 h. The presence of water vapor in the feed stream had a negative effect on the activity of $CO_2$ methanation over 5Ni/MSN. The presence of water vapor decreased the carbonyl species concentration on the surface of 5Ni/MSN, as evidenced by $CO + H_2O$-adsorbed IR spectroscopy. The RSM experiments were designed for $CO_2$ methanation over 5Ni/MSN, using FCCCD and by applying $2^4$ factorial points, eight axial points, and two replicates, with one response variable ($CO_2$ conversion). The Pareto chart indicated that the reaction temperature had the largest effect for all responses, indicating that the reaction temperature was the most important parameter in $CO_2$ methanation. The optimum $CO_2$ conversion predicted from the response surface analysis is 85% at an operating treatment time of 6 h, reaction temperature of 614 K, GHSV of 69,105 mL $g_{cat}^{-1}$ $h^{-1}$, and $H_2/CO_2$ ratio of 3.68.

## Acknowledgments

## Appendix A. Supplementary data

Supplementary data associated with this article can be found, in the online version, at http://dx.doi.org/10.1016/j.cej.2014.09.031.

## References

[1] C.H. Bartholomew, R.B. Pannell, R.W. Fowler, J. Catal. 79 (1983) 34.
[2] M.S. Batista, E.I. Santiago, E.M. Assaf, E.A. Ticianelli, J. Power Sources 145 (2005) 50.
[3] V. Jiménez, P. Sánchez, P. Panagiotopoulou, J.L. Valverde, A. Romero, Appl. Catal. A Gen. 390 (2010) 35.
[4] J.H. Kwak, L. Kovarik, J. Szanyi, ACS Catal. 3 (2013) 2449.
[5] M.A.A. Aziz, A.A. Jalil, S. Triwahyono, R.R. Mukti, Y.H. Taufiq-Yap, M.R. Sazegar, Appl. Catal. B 147 (2014) 359.
[6] S. Kiatphuengporn, M. Chareonpanich, J. Limtrakul, Chem. Eng. J. 240 (2014) 527.
[7] S. Walspurger, G.D. Elzinga, J.W. Dijkstra, M. Sarić, W.G. Haije, Chem. Eng. J. 242 (2014) 379.
[8] M.M. Zyryanova, P.V. Snytnikov, R.V. Gulyaev, Y.I. Amosov, A.I. Boronin, V.A. Sobyanin, Chem. Eng. J. 238 (2014) 189.
[9] J. Li, L. Zhou, P. Li, Q. Zhu, J. Gao, F. Gu, F. Su, Chem. Eng. J. 219 (2013) 183.
[10] M.A. Nieva, M.M. Villaverde, A. Monzón, T.F. Garetto, A.J. Marchi, Chem. Eng. J. 235 (2014) 158.
[11] M.R. Sazegar, A.A. Jalil, S. Triwahyono, R.R. Mukti, M. Aziz, M.A.A. Aziz, H.D. Setiabudi, N.H.N. Kamarudin, Chem. Eng. J. 240 (2014) 352.
[12] N.W.C. Jusoh, A.A. Jalil, S. Triwahyono, H.D. Setiabudi, N. Sapawe, M.A.H. Satar, A.H. Karim, N.H.N. Kamarudin, R. Jusoh, N.F. Jaafar, N. Salamun, J. Efendi, Appl. Catal. A 468 (2013) 276.
[13] N.H.N. Kamarudin, A.A. Jalil, S. Triwahyono, V. Artika, N.F.M. Salleh, A.H. Karim, N.F. Jaafar, M.R. Sazegar, R.R. Mukti, B.H. Hameed, A. Johari, J. Colloid Interface Sci. 421 (2014) 6.
[14] A.H. Karim, A.A. Jalil, S. Triwahyono, S.M. Sidik, N.H.N. Kamarudin, R. Jusoh, N.W.C. Jusoh, B.H. Hameed, J. Colloid Interface Sci. 386 (2012) 307.
[15] B.D. Cullity, Elements of X-ray Diffraction, second ed., Addison-Wesley, Reading, MA, 1978.
[16] D.C. Montgomery, Design and analysis of experiments, fourth ed., John Wiley & Sons, New York, 1996.
[17] J.H. de Boer, B.G. Linsen, T.J. Osinga, J. Catal. 4 (1965) 643.
[18] Y.H. Guo, C. Xia, B.S. Liu, Chem. Eng. J. 237 (2014) 421.
[19] D. Liu, R. Lau, A. Borgna, Y. Yang, Appl. Catal. A 358 (2009) 110.
[20] H. Förster, H. Fuess, E. Geidel, B. Hunger, H. Jobic, C. Kirschhock, O. Klepel, K. Krause, Phys. Chem. Chem. Phys. 1 (1999) 593.
[21] D. Murphy, P. Massiani, R. Franck, D. Barthomeuf, J. Phys. Chem. 100 (1996) 6731.
[22] O. Cairon, E. Dumitriu, C. Guimon, J. Phys. Chem. C 111 (2007) 8015.
[23] M. Primet, J.A. Dalmon, G.A. Martin, J. Catal. 46 (1977) 25.
[24] C. Guo, Y. Wu, H. Qin, J. Zhang, Fuel Process. Technol. 124 (2014) 61.
[25] T. Tatsumi, K.A. Koyano, Y. Tanaka, S. Nakata, J. Porous Mater. 1 (1999) 13.
[26] K.A. Koyano, T. Tatsumi, Y. Tanaka, S. Nakata, J. Phys. Chem. B 101 (1997) 9436.
[27] R. Kumar, P. Pal, Chem. Eng. J. 210 (2012) 33.
[28] P.D. Haaland, Experimental Design in Biotechnology, Marcel Dekker Inc., New York, 1989.
[29] I.-G. Bajusz, J.G. Goodwin Jr., J. Catal. 169 (1997) 157.